



Fracture toughness of AlSi10Mg alloy produced by LPBF: effects of orientation and heat treatment

Giorgia Lupi · Giuliano Minerva ·
Luca Patriarca · Riccardo Casati ·
Stefano Beretta

Received: 22 December 2023 / Accepted: 27 March 2024
© The Author(s) 2024

Abstract In this study, AlSi10Mg samples were manufactured by laser-powder bed fusion process to explore the fracture toughness dependence on both built orientation and aging treatment. The experiments were performed on as-built and directly-aged (200°C/4 h) conditions, with the latter revealed to be a valuable treatment for improving fracture toughness. A comprehensive investigation involving detailed microstructural analysis, grain-orientation mapping, and crack-tip strain measurements was conducted to investigate the mechanisms governing the material behavior. The results revealed that specimens subjected to direct aging display higher toughness, thereby enhancing the fracture resistance of AlSi10Mg. Moreover, a considerable variation in fracture toughness values was observed for the different printing orientations, indicating the existence of manufacturing-induced anisotropy. The findings highlight that this anisotropy mainly cor-

relates with the distinctive microstructure induced by the additive manufacturing process. In particular, this study focuses on the different preferential crack paths dictated by the melt pool boundaries orientation respective the crack propagation direction. A substantial reduction in fracture toughness was observed when the crack propagates along the melt pool boundaries.

Keywords Additive manufacturing · AlSi10Mg · Fracture toughness · Build orientation · Heat-treatment

1 Introduction

In recent years, Additive Manufacturing (AM) has experienced a growing success in engineering applications (Herzog et al. 2016; Zhai et al. 2014). Among the metal AM systems, laser-powder bed fusion (LPBF) is highly employed for manufacturing of aluminium alloys, with AlSi10Mg being largely used thanks to its good processability and specific mechanical properties. It is interesting to highlight that LPBF parts can often perform better than the wrought counterpart, in particular in terms of tensile strength and fracture toughness, see for example (Kempen et al. 2012; Aboulkhair et al. 2019). However, the anisotropy of the mechanical properties induced by the LPBF process requires particular attention, due to the presence of weak orientations. For a widespread industrial application of LPBF for the production of structural components, it is then of paramount importance to further investigate the

G. Lupi · G. Minerva · L. Patriarca (✉) · R. Casati · S. Beretta

Department of Mechanical Engineering, Politecnico di Milano, Via La Masa 1, Milan 20156, Italy
e-mail: luca.patriarca@polimi.it

G. Lupi
e-mail: giorgia1.lupi@polimi.it

G. Minerva
e-mail: giuliano.minerva@polimi.it

R. Casati
e-mail: riccardo.casati@polimi.it

S. Beretta
e-mail: stefano.beretta@polimi.it

microstructural mechanisms governing the static fracture of the AlSi10Mg alloy for specific orientations, in order to design tailored heat-treatments or specific laser scanning strategies. This work aims to fully investigate the origin of the fracture toughness anisotropy through microstructural investigation of crack paths for as-built and directly-aged LPBF specimens.

For AMed parts, the layer-by-layer deposition process induces a significant anisotropy in mechanical properties. In the work of AlRedha et al. (2020), AlSi10Mg specimens were produced by LPBF along different directions and then tested in the as-built condition. The lowest fracture toughness was obtained in vertically built parts with the crack surface orthogonal to the building direction, while horizontally printed specimens exhibited the highest toughness values. This observation aligns with findings by de Menezes et al. (2019) on A357 material tested in as-built and aged (160°C for 4 h) conditions. The authors correlated the variation in fracture response to the presence of melt pool boundaries (MPBs). The significant reduction in fracture toughness was attributed to the ease for cracks to propagate through the MPBs. The influence of MPBs on the mechanical properties of 316L LPBF parts was also analysed in the work of Shifeng et al. (2014). The authors correlated the anisotropy in the properties of the material with the presence and distribution of MPBs. The MPBs between tracks are the main factor that causes the fracture of printed parts, thus a large quantity of such interfaces on the same cross-sectional area is responsible for increasing the probability of cracking. An additional critical aspect that can considerably influence strength and toughness of LPBF-AlSi10Mg parts is the presence of residual stresses. Different heat-treatment routes can be employed to mitigate residual stresses and improve or homogenize mechanical properties. These include stress relief heat-treatment, solution treatment followed by water quenching and artificial aging (T6 temper), and direct aging from the as-built state (T5 temper), as discussed by Takata et al. (2017). Several studies on the beneficial effect of stress relief on fracture toughness have been published in recent years, Araújo et al. (2021); Rosenthal et al. (2018). However, such heat-treatment leads to a significant decrease in monotonic properties, Li et al. (2016). In their study, Brandl et al. (2012) demonstrated that for AlSi10Mg samples printed in different orientations and subjected to various post-heat-treatment processes, heat-treatment had the most substantial impact

on fatigue and fracture behavior. In contrast, the orientation of the samples exhibited the least significant influence on these mechanical properties.

The beneficial effect of a direct aging heat-treatment on the mechanical properties has been proven by several studies. Specifically, direct aging of as-built LPBF-AlSi10Mg has been widely adopted to form fine strengthening precipitates, Zhao et al. (2022); Park et al. (2021). This study investigates the effects of a novel direct aging process conducted at 200°C for 4 h on the fracture toughness properties of the AlSi10Mg alloy. The research places particular emphasis on the examination of various build orientations. These findings hold significant relevance from an industrial perspective, given that AlSi10Mg alloys are highly suitable for manufacturing across a wide range of applications.

In particular, this study explores the impact of direct aging on fracture toughness through the examination of specimens printed in three build orientations: horizontal (H), vertical (V), and diagonal (D). A detailed microstructure analysis, incorporating Kernel Average Misorientation (KAM) maps, has been employed to study the crack propagation path. Lastly, Digital Image Correlation (DIC) measurements were used to identify the extension of the crack tip plastic zone through the equivalent Tresca strain.

2 Materials and methods

2.1 Specimen manufacturing

AlSi10Mg Compact Tension (CT) specimens were manufactured by LPBF process. The powder used to fabricate the specimens was produced by ECKA Granules. It showed a $D_{10}=21\mu\text{m}$, $D_{50}=37\mu\text{m}$, and $D_{90}=65\mu\text{m}$. The nominal composition of the powder is reported in Table 1.

LPBF was performed by a SLM 280HL v1.0 system equipped with two 400 W Yttrium fibre lasers in a build chamber of 280x280x350 mm³ (SLM Solution Group AG). The build chamber was flooded with argon to reach oxygen levels lower than 0.2% during the printing process. The process parameters were the following: beam power $P=350\text{ W}$, hatch distance $h=0.13\text{ mm}$ and scan speed $v=1650\text{ mm/s}$. The layer thickness was $t=50\mu\text{m}$ and produced a fluence $\mathcal{F}=32.63\text{ J/mm}^3$. The building platform was pre-heated up to 150°C. The scan

Table 1 Chemical composition (wt%) of AlSi10Mg powder

Al	Si	Fe	Cu	Mn	Mg	Ni	Zn	Pb	Sn	Ti	Others
Balance	10	0.55	0.05	0.45	0.325	0.05	0.10	0.05	0.05	0.15	0.15

strategy adopted stripes rotated by 67° after each layer and the scanning order was to first create two contours and then perform the hatch scanning.

Tensile behaviour of the AlSi10Mg alloy in both as-built (AB) and heat-treated (HT) conditions was characterised using standard specimens in air and at room temperature. Three specimens for each combination of heat treatment and orientation were employed, except for the heat-treated samples in D direction for which only one specimen was available. Tensile specimens were printed in near net shape conditions, with only their ends machined to ensure a precise alignment with the testing machine. Data of the material in the as-built condition was published by [Minerva et al. \(2022\)](#) and is herein reported to provide a direct comparison. The tensile tests were performed on cylindrical specimens according to the ASTM E8 standard ([ASTM 2021](#)) on an MTS Alliance RT 100 load frame, equipped with a 100 kN load cell. The strain was measured with an MTS extensometer with 8 mm gauge length. The selected specimens geometries were cylindrical with gauge diameter of 3 mm. Tensile specimens were sized according to the ASTM E8/E8M standard test method for tension testing of metallic materials ([ASTM 2021](#)). The geometry of the fracture toughness specimens is reported in [Fig. 1a](#) along with the nominal dimensions selected according to the ASTM E1820 standard ([ASTM 2020](#)). The thickness of the specimens was $B=12.4$ mm, while the width to thickness ratio was $W/B=2$. The notch depth was approximately 12 mm. Three orientations were investigated (H, V, and D) as shown in [Fig. 1](#). Some specimens were tested in the as-built condition, while the others were heat-treated by a direct aging performed at 200°C for 4 h. [Table 2](#) reports the overall number of specimens per condition and orientation.

2.2 Fracture toughness tests

The fracture toughness tests were conducted according to the ASTM E1820 standard ([ASTM 2020](#)) employing the resistance curve (R-curve) method. Before testing,

all specimens were subjected to fatigue load cycling with decreasing Stress Intensity Factor (SIF) range ΔK at constant load ratio $R=0.1$ to produce fatigue cracks with a length of approximately 2 mm. The crack length was measured on specimens' lateral surfaces with a Zeiss light optical microscope (LOM). To obtain a clear image of the crack, the lateral surfaces were polished with sandpaper up to a grit of P2500. The tests were carried out in load control on an MTS 810 machine equipped with a 10 kN load cell and an MTS clip-on gauge with a nominal length of 5 mm. During the test, the region of crack propagation was monitored by means of 2D Digital Image Correlation (DIC), using a 2 Megapixel Allied Vision Manta CCD camera equipped with a lens system produced by Navitar. A speckle pattern was applied to one lateral surface of each specimen by means of an Iwata airbrush, as described in [McNeill et al. \(1987\)](#). The region of interest ahead of the crack tip measured approximately 5×6.5 mm², the images were acquired with a final resolution of 4 $\mu\text{m}/\text{pixel}$. Correlation of the images was performed with the VIC 2D correlation software by Correlated Solutions using square subsets with a side of 47 pixels spaced by 1 pixel. The reference image was taken at the beginning of each test, after the specimen was mounted and subjected to a tensile load of 100 N, to guarantee the alignment with the load axis of the testing machine. During the test, images of the region of interest were captured at intervals of 0.5 s, synchronized with the signal acquisition of load, crack mouth opening displacement, and the crosshead displacement.

The fracture toughness tests were stopped after 1.5 mm of stable crack advancement, measured by the clip-on gauge, thus avoiding complete specimen failure. After the tests, the specimens were subjected to additional fatigue loading to mark the crack front. The fatigue cycling was performed at constant load ratio $R=0.1$, with load range equal to half of the final load of the test $\Delta F = F_{fin}/2$, up to the condition of unstable crack propagation. Subsequently, images of the fracture surfaces were captured using the same microscope previously described for the DIC measurements. The result-

Fig. 1 (a) CT specimens main nominal dimensions (in mm) (b) Schematic representation of the LPBF specimens in the three building directions

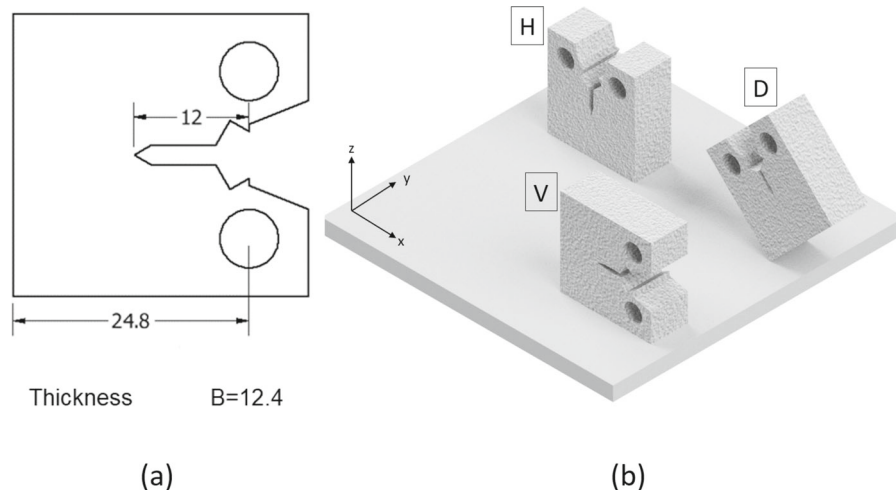


Table 2 Summary of all the printed samples

AB H	AB V	AB D	HT H	HT V	HT D
2	2	2	4	2	4

ing fractographies were used to measure the pre-crack and the final crack lengths after specimens' failure.

2.3 Microstructure analysis

The relative density of the samples was reported in a previous work of the authors, see (Minerva et al. 2022). The relative density was 99.1%, measured according to ASTM B962 (ASTM 2017). To study the crack paths and investigate the differences between the as-built and heat-treated condition, the specimens were sectioned along the midplane of the specimen's thickness, orthogonally to the crack propagation plane. The samples were then etched using Keller's reagents to analyse the melt pools with a LOM and the microstructure with a field emission scanning electron microscope (SEM). The LOM used was an Eclipse LV150NL with lenses from 25X to 1000X, while the SEM was a Zeiss Sigma 500, equipped with Oxford Instruments Ultim Max for energy dispersive X-ray analysis (EDS) and with an Oxford Instruments' electron backscatter diffraction (EBSD) detector, model C-Nano. EBSD maps were acquired from non-etched samples and the obtained data was processed and analyzed by Tango software to study intensification of local strains with KAM maps.

2.4 Finite element modelling

For a deeper understanding of the plastic tip region, Finite Element (FE) analyses and DIC strain measurements were conducted, followed by a comparative assessment. Specifically, in-plane strain measurements were employed with the aim of delineating the extent of the plastic zone at the crack tip. The true stress–true plastic strain curves obtained from the tensile tests were used to model elastic–plastic material properties for each orientation and condition (as-built or heat-treated) in Dassault Systèmes' Abaqus. A plane stress model with thickness equal to 12 mm was designed to simulate the free surface condition captured by DIC. Each specimen's hole was kinematically coupled to a reference point at its center, leaving only the rotational degree of freedom unconstrained. The lowermost reference point was then constrained in both horizontal and vertical directions, thus acting as a pin, while the uppermost reference point was constrained in the x direction, acting as a roller. A circular partition was created at the crack tip, to obtain a regular mesh with quadratic wedge and quadrilateral elements. The rest of the model was meshed with quadratic quadrilateral elements with average size equal to 200 μm. The load was applied in the vertical direction on the uppermost reference point in a step-wise manner and the J-integral was computed at the maximum load of 1 kN. The FE strains were post-processed to obtain the equivalent Tresca strain. For a 2D case, the Tresca equivalent strain is calculated as:

$$\varepsilon_{GT} = \frac{\varepsilon_1 - \varepsilon_2}{1 + \nu} \quad (1)$$

Table 3 Fracture toughness mean values and scatter of this AlSi10Mg alloy as J_Q for each condition and orientation

Fracture Toughness J_Q [N/mm]	Orientation		
	H	V	D
AB	9.1±0.2	4.3±0.6	3.4±1.2
HT	9.9±0.7	5.5±0.3	4.0±0.7

ε_1 and ε_2 are, respectively, the first and second principal strains. As a matter of comparison with the DIC strains, we should notice that in the experiments no information on ν can be provided to the correlation software and it calculates modified Tresca strains as:

$$\varepsilon_{GT}^* = \varepsilon_1 - \varepsilon_2 \quad (2)$$

The modified Tresca strains were generated from the principal strain fields output using Eq. 2, in order to be comparable with the correlated images. The plastic zone $r_{p, FEM}$ was measured for a modified Tresca strain equal to 0.5%.

3 Experimental results

3.1 Mechanical testing

3.1.1 Fracture toughness tests

Figure 2a, b show the R-curves obtained with CT specimens for the as-built and directly-aged conditions. The blue R-curves were obtained for the H orientation, the green and red R-curves for the D and V, respectively. The dashed black lines corresponds to the blunting lines shifted by $\Delta a=0.2$ mm and their intersections with the R-curves represent the J_Q values, reported in Fig. 2c and Table 3.

It is important to point out that the optically measured physical crack lengths did not conform to the prescriptions on the crack front shape contained in the ASTM E1820 (ASTM 2020) standard, hence the J_Q values could not be strictly qualified as J_{IC} . Non-conformity of the crack front shapes may be related to the absence of side-grooves on the CT specimens. However, it should be noted that the side-grooves were not machined to allow the DIC measurements performed on the specimens requiring flat lateral surfaces. Nonetheless, the values of J_Q obtained were comparable to J_{IC} values in the literature (Liu et al. 2020; Paul et al. 2021; Araújo et al. 2021), therefore, J_Q values

were used as the reference material fracture toughness. From fracture toughness results, two different effects, one related to the direct aging heat-treatment and one to the printing orientations, could be deduced. The heat-treatment was found to have a beneficial effect on toughness properties of the material, leading for all the orientations to higher fracture toughness values. In addition, heat-treated specimens all show a significantly larger increase of resistance to crack growth over the nominal fracture toughness J_Q (R-curve). This is particularly relevant for V specimens, which have a very slow increase of J versus Δa in the as-built condition, and the R-curve almost horizontal for $\Delta a=2$ mm. On the other hand, for the heat-treated condition the crack resistance at $\Delta a=2$ mm is more than double with respect to the measured J_Q . The same effect can be also appreciated for H specimens, while it is less significant for D specimens. On the other hand, the different values of fracture toughness between the samples with different build direction indicates the existence of anisotropy in the resistance to static fracture advancement. In both as-built and heat-treated conditions, the H samples have the highest fracture toughness, followed by the V and the D samples. To the Authors' best knowledge, the only two studies on fracture toughness of AlSi10Mg produced by LBPF with orientations 0° , 45° and 90° showed a similar trend. In Araújo et al. (2021) and Hitzler et al. (2019), the highest fracture toughness is shown by the 0° orientation (which corresponds to H direction in this study), while the lowest fracture toughness was found for the 90° orientation. The 45° orientation displayed intermediate values, close to the 90° orientation (which corresponds to H direction in this study). In the present case, V and D showed a similar behavior, with D-printed samples exhibiting slightly lower values of J_Q .

3.1.2 Tensile tests

The monotonic properties obtained from the tensile tests are reported in Fig. 3. Table 4 shows a comparison between tensile and fracture toughness properties from the literature and the present study. Regarding the monotonic properties, Table 4 reports the yield strength $R_{p,0.2\%}$, the ultimate tensile stress R_m , the strain at failure ε_f and the strain hardening exponent n . The strain hardening exponent n was obtained by a least-squares fitting of the Ramberg-Osgood equation (Dowling 2013):

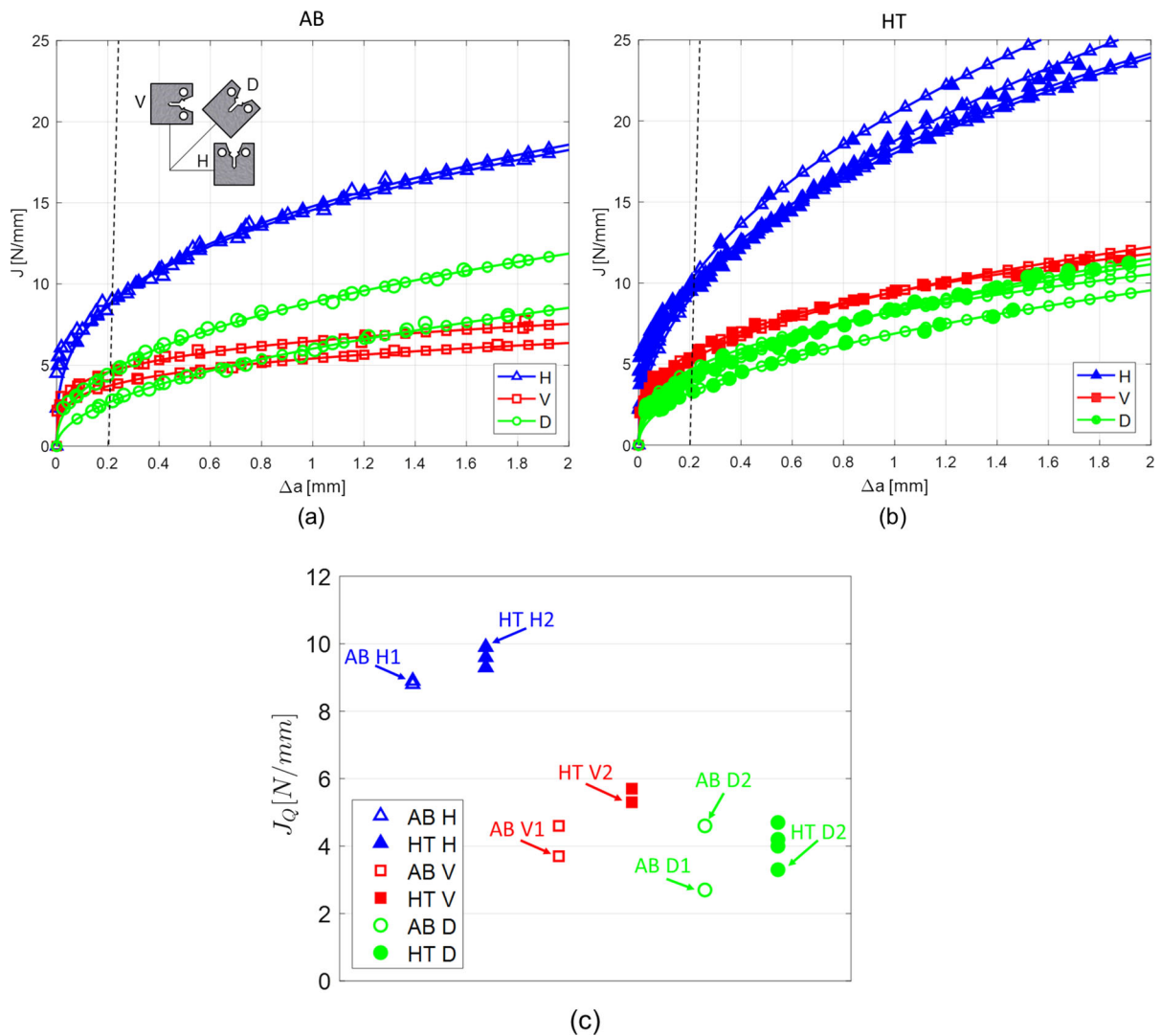


Fig. 2 R-curves obtained using CT specimens for **a** AB, **b** HT condition. **c** J_Q values for all the specimens, samples that have been microstructurally analysed are highlighted

$$\varepsilon = \frac{\sigma}{E} + 0.002 \left(\frac{\sigma}{R_{p,0.2\%}} \right)^{1/n} \quad (3)$$

Concerning the direct aging carried out in this study, it is possible to notice that the H and D heat-treated samples showed a slight decrease in the R_m . Previous studies indicated that direct aging of the AlSi10Mg alloy performed at a lower temperature (160°C, 4 h) than that used in this work resulted in higher R_m and $R_{p,0.2\%}$ compared to the as-built condition of the material (Casati et al. 2018). On the other hand, Tang et al. (2023) examined the impact of direct aging on the AlSi10Mg alloy and noted that when the temperature

was raised to 200°C, the peak aging occurred at 1 h, after which the hardness and tensile properties rapidly declined. When aging is performed at 160°C, the peak aging time is 3 h, and the subsequent mechanical properties decreased slowly. The authors attributed this difference in peak aging time to the sluggish diffusion of solute atoms, retarding the formation of Mg-Si precipitates. The overaging performed on AlSi10Mg samples in this work (200°C, 4 h) is likely to induce a reduction in residual stresses as well (Casati et al. 2021). It is also worth mentioning that proper overaging treatment could reduce the anisotropy of the mechanical

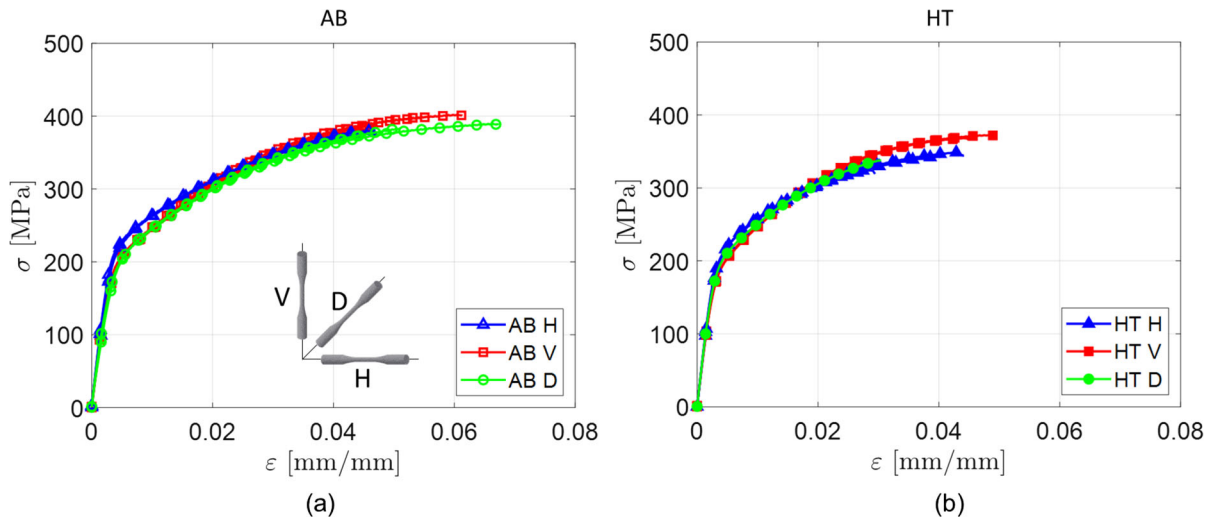


Fig. 3 Tensile curves obtained on tensile specimens manufactured alongside CT specimens for **a** AB (Minerva et al. 2022), **b** HT condition

properties of the alloy, thus resulting in a better combination of mechanical properties in transverse and longitudinal direction (Tang et al. 2023). Moreover, it is possible to note that tensile properties became worse upon heat treatment, while the fracture properties actually improved (Table 4). Indeed, it has been reported in literature that toughness properties are less sensitive to heat treatment than tensile properties (Araújo et al. 2021).

3.2 Microstructural analyses

In Fig. 4, SEM images from the mid-sections perpendicular to the crack plane are reported. In the as-built condition, the AlSi10Mg alloy shows the typical cellular-like solidification structure consisting of Al cell decorated at boundaries by eutectic Si particles. In the heat-treated sample, the cellular structure is maintained, and small precipitates are noticeable at the core of cells. Menezes et al. (2022) reported that the cracks preferably propagate along solidification cells, where eutectic Si particles are mainly segregated. In this work, despite the presence of Si-rich intercellular regions, the cracks do not show a tendency to propagate preferentially along these regions, but they randomly break the Al cell. However, the fine dispersion of precipitates within cells is responsible for an increase in fracture toughness via precipitation hardening, as also confirmed by the work reported in ref (Ahn et al.

2022). Moreover, in the study of Tang et al. (2023), it was demonstrated that direct aging heat treatment (160°C, 4 h) can remove part of the residual stress in the AlSi10Mg alloy (about 40% of the residual stress), with a positive effect on fracture toughness.

To investigate anisotropy in fracture toughness, fracture surfaces of specimens were analysed with SEM and are shown in Fig. 5. Across all cases, it is possible to discern distinct regions on the fracture surfaces, including fatigue pre-crack zones, stable crack growth regions, and areas characterized by unstable crack propagation. Moreover, it was observed the presence of crack tunneling in all specimens. In the case of vertically printed parts, discernible traces of the scan track are detectable. To gain deeper insights into crack propagation and its correlation with the local microstructure, the mid sections of the specimens underwent examination using an optical microscope. The reconstructed crack paths for the H, V, and D samples are illustrated in Fig. 6, with particular emphasis on the stable crack growth regions found in all analyzed samples. In H samples, the crack propagates through the melt pool without following any specific path. Occasionally, the crack changes direction, primarily along the weaker boundaries between melt pools. In contrast, in both V and D samples, the crack proceeds along the melt pool boundaries that are favorably oriented with respect to the crack plane. This preferential path has a pronounced impact on fracture toughness; when an easily traversable route for

Table 4 Average material properties of the AlSi10Mg alloy processed by LPBF for different orientations and conditions in the literature. The values reported in the table refer to similar printing parameters adopted in this work

	Condition	Orientation	Monotonic				Fracture J_{mat} [N/mm]
			$R_{p,0.2\%}$ (YS) [MPa]	R_m (UTS) [MPa]	ϵ_f [%]	n	
Minerva et al. (2022)	AB	H	229±4	379±2	4.7±0.4	0.144	9.1
		V	208±1	396±8	5.4±0.7	0.202	4.3
		D	206±3	383±8	5.4±1.1	0.196	3.5
(this study)	HT	H	219±1	339±13	3.9±0.7	0.152	9.9
		V	202±0	370±2	4.7±0.3	0.206	5.5
		D	210	338	3.5	0.192	4.0
Liu et al. (2020)	AB	H	229	389	6.3	–	9.9
Paul et al. (2021)	AB	H	190	323	6.7	–	10.4
		V	214	340	3.2	–	6.1
Araújo et al. (2021)	AB	H	266	413	5.6	–	8.4
		V	243	352	2.8	–	6.0
		D	249	382	3.6	–	–
	SR	H	230	350	7.2	–	11.4
		V	212	337	5.7	–	10.4
		D	190	292	8.2	–	15.5

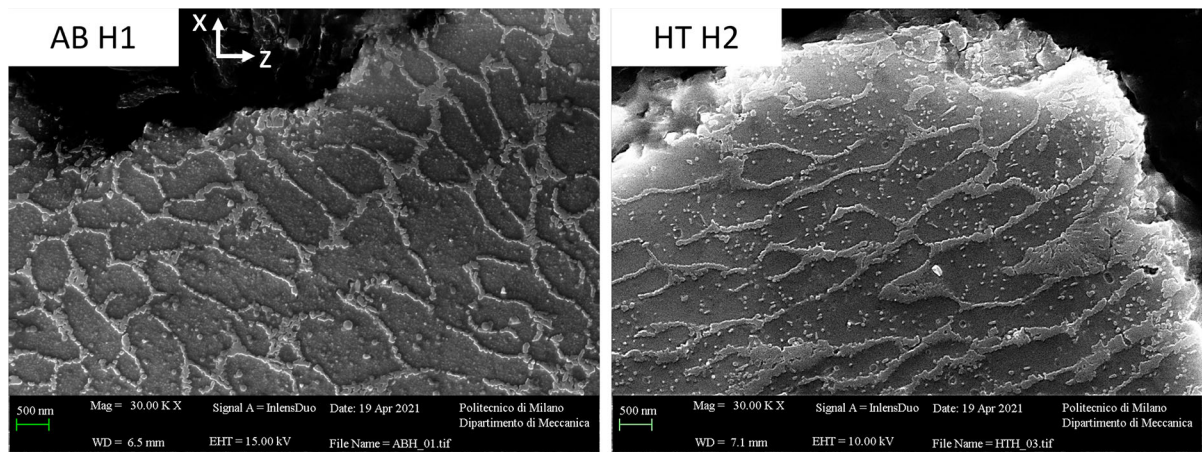


Fig. 4 SEM images from the mid-sections perpendicular to the crack plane (Z-X plane) in the stable crack growth region of the horizontal specimens in as-built and heat-treated conditions

the crack is present, the fracture toughness tends to decrease.

By comparing SEM images of the fracture surfaces in the stable crack growth regions, secondary cracks are visible in the V sample (Fig. 7a, b). The correlation between tortuous crack paths and secondary cracks formation on mechanical properties has been widely studied for welds. It has been found that where the

crack changes its path (i.e., forming a tortuous crack path), secondary cracks are frequently formed. Secondary cracks can delay the crack growth rate by reducing the energy at the crack tip (Jang et al. 2010; Xu et al. 2019; Zhang et al. 2020; Trudel et al. 2014). Therefore, a very tortuous crack path can be correlated to a higher fracture toughness due to the formation of secondary cracks. This observation suggests that while

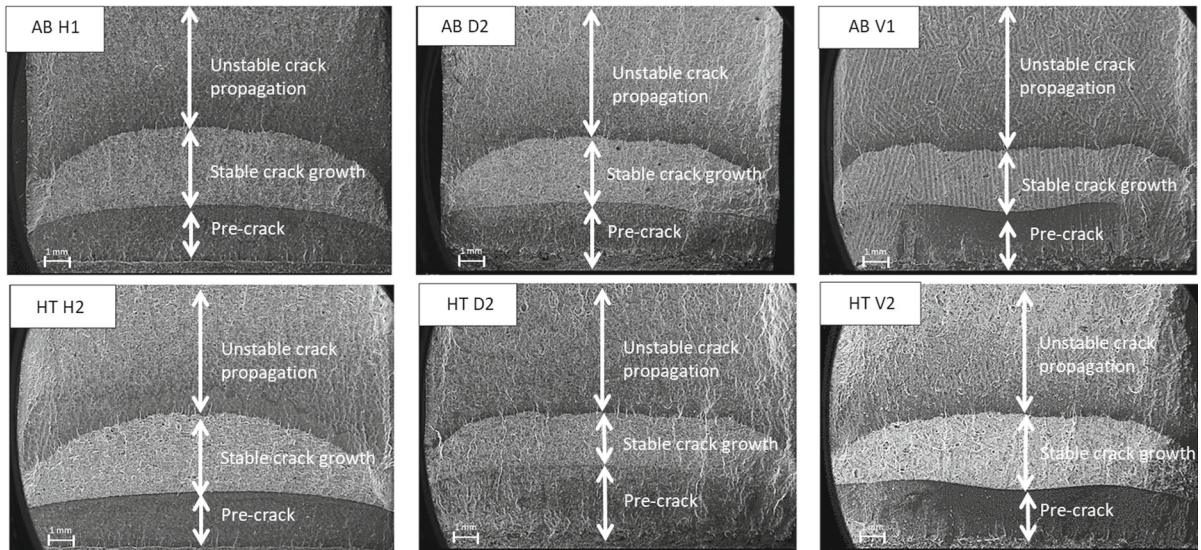


Fig. 5 SEM images of the fracture surfaces

preferential crack paths contribute to fracture toughness anisotropy, the emergence of secondary cracks is an additional factor influencing this material property. This insight provides a basis for understanding why vertical samples exhibit superior performance compared to diagonal ones.

Regarding the heat-treated samples, the results show better performance in terms of fracture toughness than the as-built samples. One beneficial effect can be related to the fine Si precipitates in the Al cell. Moreover, we also observed a more tortuous fracture path generally associated with the material in the heat-treated condition. As an example, the crack path of the heat-treated horizontal sample is more tortuous than that of the as-built material (Fig. 6) and, as a consequence, secondary cracks are clearly visible in the SEM images of the fracture surfaces (Fig. 7c, d). The more tortuous fracture path that characterizes the horizontally produced samples is clearly identifiable from fractographic analysis due to the presence of many variations in depth of the fracture plane together with other flatter areas, as suggested by Girelli et al. (2019). In this scenario, the fracture toughness of the heat-treated samples is still mainly controlled by the presence and distribution of the MPBs, as in the case of the as-built samples.

In Fig. 8, a schematic illustration depicting the preferential crack paths for all orientations is presented. Furthermore, Electron Backscatter Diffraction (EBSD)

maps were conducted in the stable crack growth regions to provide additional insights into the characteristics of crack propagation. MPBs were discerned by overlaying images of the identical area captured with an optical microscope after the samples underwent etching. It is possible to observe that melt pools have not a uniform shape throughout the microstructure due to the rotation of the scanning direction by 67° between successive layers. This scan strategy allows to reach higher toughness values since it results in randomly distributed melt pools that promote more tortuous crack propagation paths (Zhao et al. 2022; Suryawanshi et al. 2016).

EBSD maps also show that several grains grow epitaxially at the layer-layer MPBs, while at track-track MPBs smaller grains with an equiaxed structure are found. The epitaxial growth of grains makes the layer-layer MPBs stronger than track-track MPBs (Xiong et al. 2019). These differences in the bond between two types of boundaries could affect the mechanical properties of the printed materials. In the present V samples we observe that the crack tends to propagate mostly through layer-layer melt pool boundaries, while, in D samples, track-track melt pool boundaries are mostly involved. This could further contribute to the higher fracture toughness of V samples than that of D samples where the MPBs have a lower bonding.

EBSD maps were analyzed to generate Kernel Average Misorientation (KAM) maps, as illustrated in Fig. 9. The level of local misorientation is correlated with the

Fig. 6 Crack profiles and stable crack growth regions of the analysed samples tested in as-built and heat-treated condition for the orientation: **a** horizontal, **b** vertical and **c** diagonal

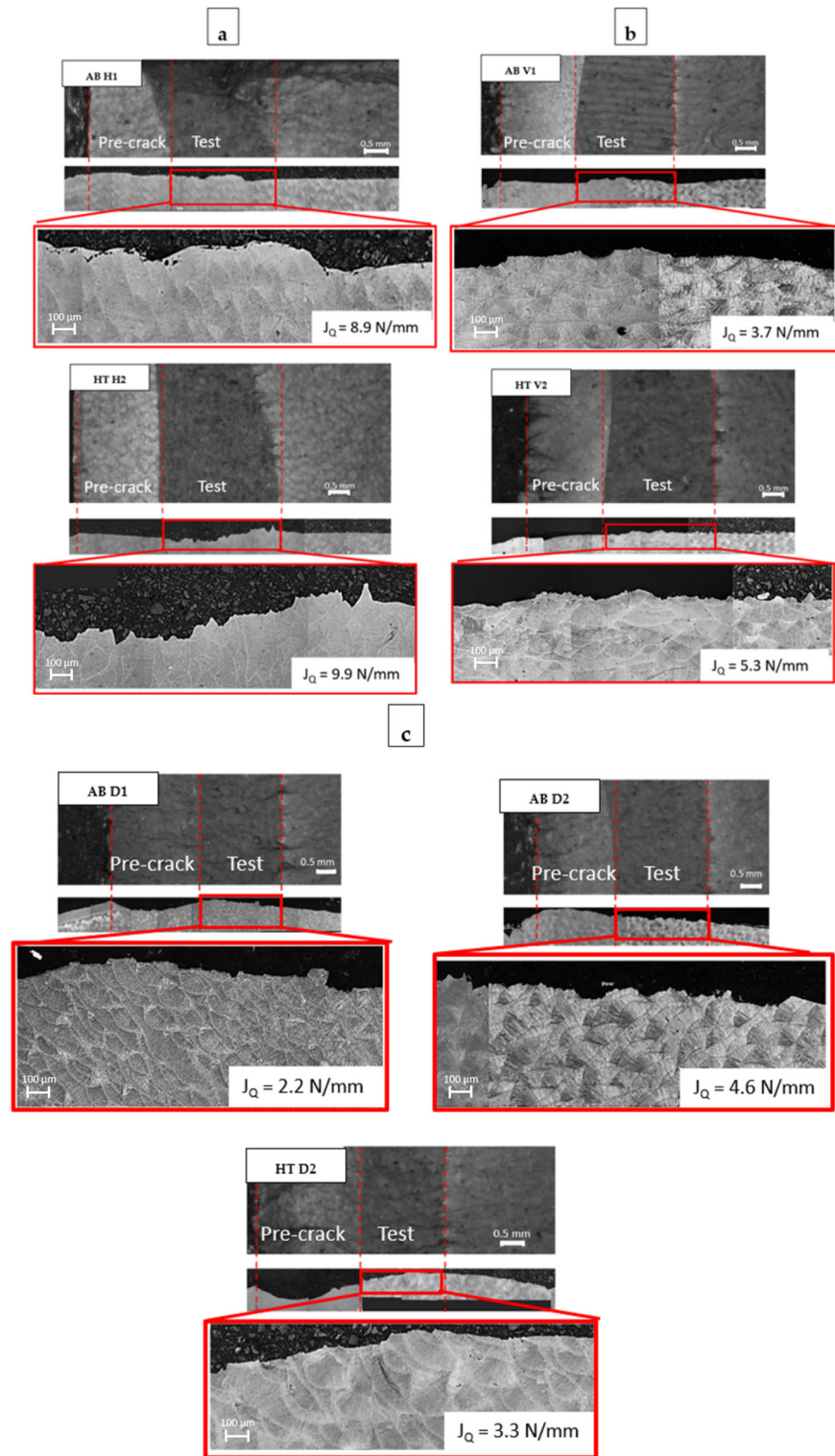
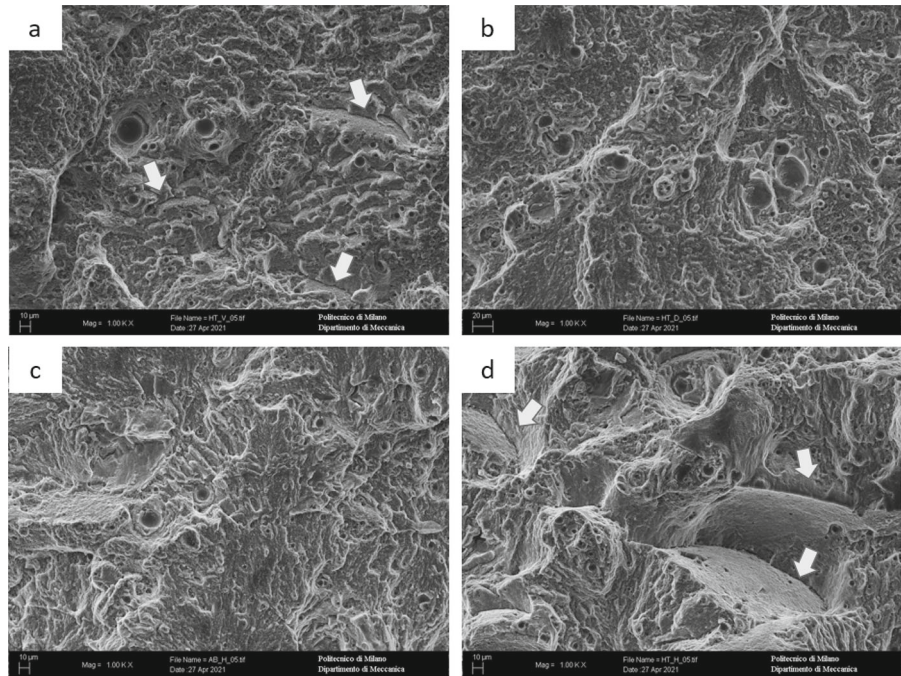


Fig. 7 SEM images of the fracture surfaces of **a** HT V2, **b** HT D2, **c** AB H1 and **d** HT H2. White arrows indicate the presence of secondary cracks



level of residual strains. In the color bar of Fig. 9, the green color indicates a high level of local misorientation which indicates high residual strains, whereas the blue color marks a lower concentration of residual strains. The local misorientation is thus an index of the local energy dissipated at the crack tip during the stable crack advancement.

The H specimens exhibit a marked presence of local residual strains compared to both V and D specimens. However, we remark that the monotonic stress–strain behavior is similar for all orientations and heat treatments. This suggests that the large presence of residual strains observed in the H specimens results from higher fracture toughness in this orientation resulting from the microstructural barriers that hinder crack advancement. An increased in external load is thus necessary for the crack to propagate, leading to larger plastic tip radius and leading to higher residual local strains as detected by KAM.

The KAM maps of the AB V1 and AB D1 do not show relevant differences among them. By comparing the two diagonal printed samples, the AB D1 sample shows a slightly lower deformation nearby the crack propagation path than the AB D2. In the AB D2 case, a small misorientation along the crack path was noted, this is indicative of strain localization without general plastic deformation throughout the entire grain. This

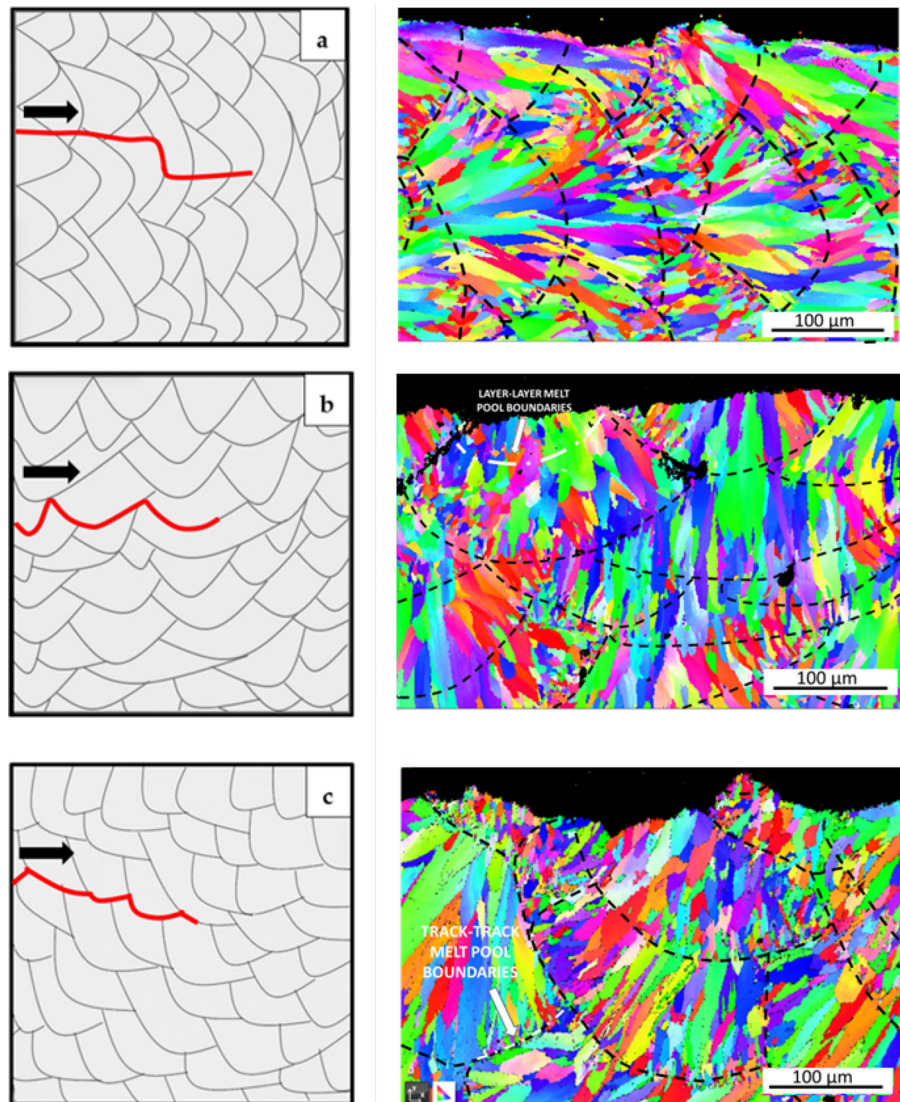
difference in the surface deformation could explain the variations in the fracture toughness values of the two samples printed in the same direction, indeed the AB D1 sample has a slightly lower J_Q value.

4 Crack tip plasticity

DIC measurements, supported by FE simulations, were performed to investigate the size and shape of the crack-tip plastic region. All the DIC strain maps were compared at the point of J_Q on the R-curves corresponding to a stable crack advancement of 0.2 mm. Correlated images of the as-built specimens investigated with KAM and a selection of heat-treated specimens are featured in Fig. 10. The strain maps show the equivalent Tresca strain, while the FE simulations are reported in terms of plastic tip contour by a dashed white line.

The figures illustrate that the plastic zones are notably larger for the H orientation specimens, aligning with the extensive deformation observed on the fracture surfaces in KAM images. The enhanced fracture resistance associated with the H orientation enables a greater portion of the material in the crack tip region to undergo plastic deformation. Figure 10 also shows that the plastic zones computed with FE analyses correspond with the measured ones. Moreover, the symmetric plastic

Fig. 8 Schematic representations of the crack path and EBSD maps for AB samples: **a** horizontal, **b** vertical and **c** diagonal



zones obtained with DIC allows to conclude that the material shows no significant anisotropic stress–strain behaviour and that the differences observed in the fracture toughness properties are due to the different crack propagation paths, as described in Sect. 3. A small deviation from a symmetric plastic tip region is only observed for the D specimens. This behavior can be correlated with a tilted crack that does not follow the symmetry plane of the specimen (Fig. 8c) also inducing a mode II crack advancement other than a pure mode I.

5 Concluding remarks

Fracture toughness of LPBF-AlSi10Mg specimens was investigated in this study focusing on the effects of orientation and heat treatment. The work supports the following conclusions:

- Fracture toughness is lower when the crack follows the melt pool boundaries as in the case of vertical and diagonal samples. The type of melt pool boundaries (layer-layer or track-track) also affects fracture toughness. In layer-layer melt pool boundaries

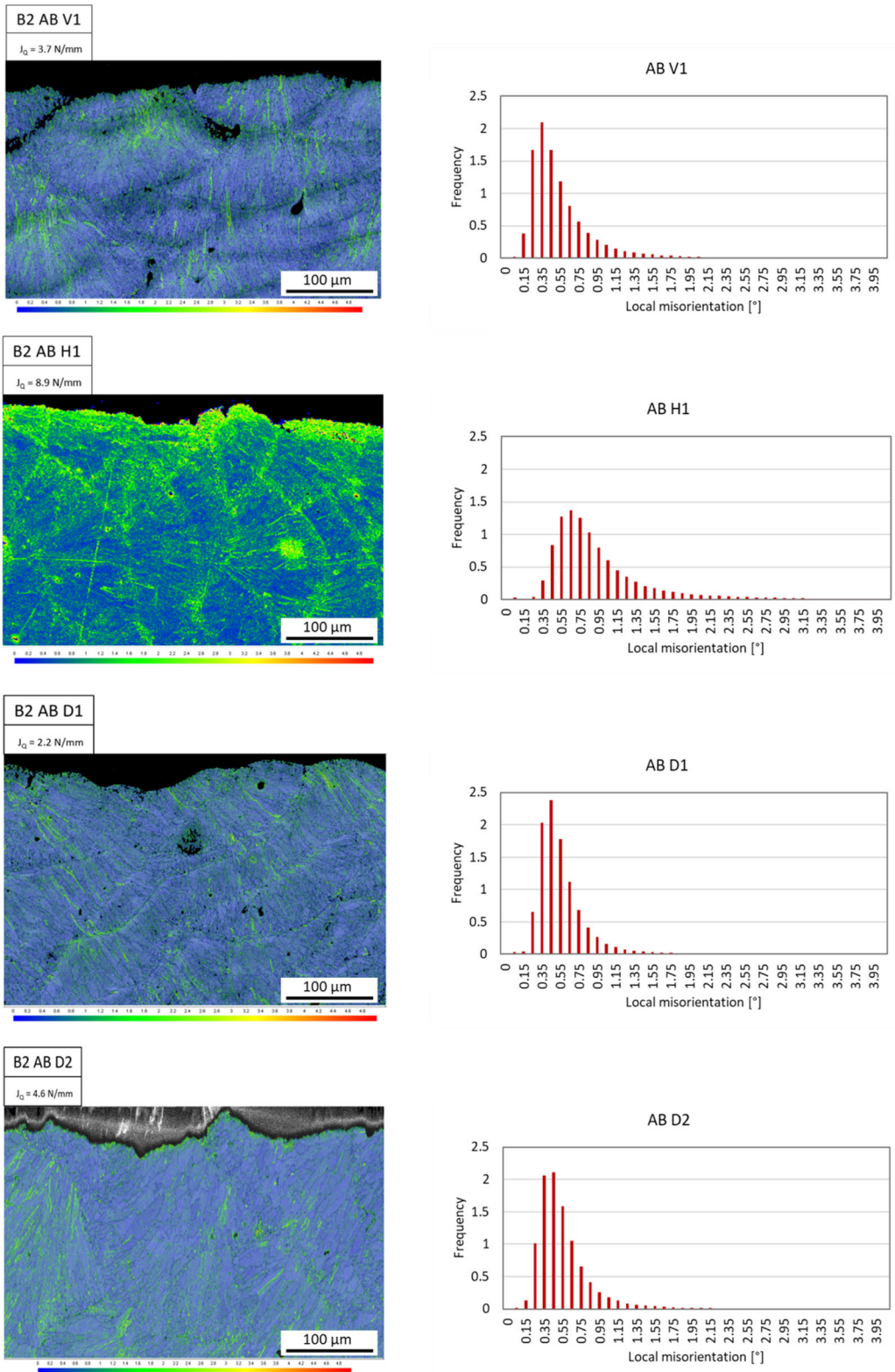


Fig. 9 KAM maps of AB samples. Green color indicates high strain concentration, while blue color represents low strain concentration

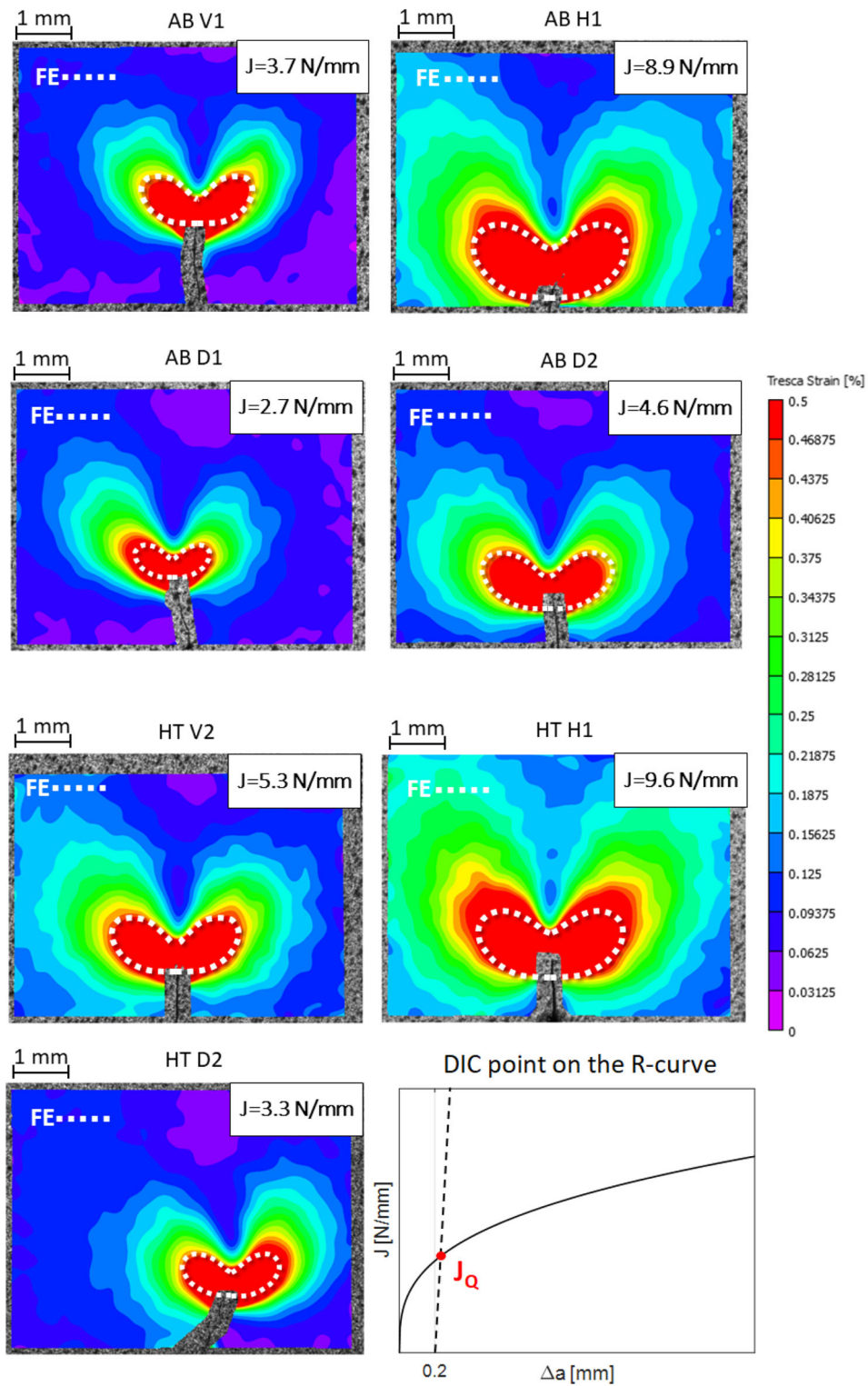


Fig. 10 DIC images of the Tresca strain near the crack tip on the surfaces of the as-built specimens analysed with KAM and a selection of heat-treated specimens

the bonding force is higher and, as a consequence, fracture toughness is higher if the crack propagates mostly along this kind of melt pool boundaries. For this reason, fracture toughness is higher when the crack propagates mostly along layer-layer melt pool boundaries, as in the case of vertical printed samples.

- A tortuous crack path and the formation of secondary cracks were associated to higher values of fracture toughness. Indeed, the crack deflection that occurs results in lowered crack driving force at the crack tip.
- An increase in the level of plastic deformation means that the crack propagation occurs through less favorably oriented grains denoting that higher fracture surface deformation relates to higher fracture toughness.

All these considerations are both valid for as-built and heat-treated samples, as demonstrated by the DIC observations, as well as by the FE simulations. However, the direct aging treatment used in this study was found to have a beneficial effect on the toughness properties of the material leading to higher fracture toughness values for all the heat-treated specimens with respect to the counterpart printed in the same direction, but tested in the as-build condition.

Author contributions G.L. and G.M. wrote the main manuscript test. G.L. conducted microstructural investigations (SEM, EBSD, crack paths). G.M. and L.P. conducted the fracture toughness tests and performed the DIC strain measurements. R.C. and S.B. developed the initial concept of the research, provided the founding and supervised all the activities. All the authors reviewed the manuscript.

Funding Open access funding provided by Politecnico di Milano within the CRUI-CARE Agreement.

Data Availability No datasets were generated or analysed during the current study.

Declarations

Conflict of interest The authors declare no Conflict of interest.

Open Access This article is licensed under a Creative Commons Attribution 4.0 International License, which permits use, sharing, adaptation, distribution and reproduction in any medium or format, as long as you give appropriate credit to the original author(s) and the source, provide a link to the Creative Commons licence, and indicate if changes were made. The images or other third party material in this article are included in the article's Creative Commons licence, unless indicated otherwise in a credit line to the material. If material is not included in the article's Cre-

ative Commons licence and your intended use is not permitted by statutory regulation or exceeds the permitted use, you will need to obtain permission directly from the copyright holder. To view a copy of this licence, visit <http://creativecommons.org/licenses/by/4.0/>.

References

- Aboulkhair NT, Simonelli M, Parry L, Ashcroft I, Tuck C, Hague R (2019) 3d printing of aluminium alloys: Additive manufacturing of aluminium alloys using selective laser melting. *Prog Mater Sci* 106:100578
- Ahn SY, Moon J, Choi YT, Kim ES, Jeong SG, Park JM, Kang M, Joo H, Kim HS (2022) A precipitation-hardened alsi10mg alloy fabricated using selective laser melting. *Mater Sci Eng, A* 844:143164
- AlRedha S, Shterenlikht A, Mostafavi M, Van Gelderen D, Lopez-Botello OE, Reyes LA, Zambrano P, Garza C (2020) Effect of build orientation on fracture behaviour of alsi10mg produced by selective laser melting. *Rapid Prototyping Journal*
- Araújo LC, Gabriel AHG, Fonseca EB, Avila JA, Jardini AL, Junior RS, Lopes ÉSN (2021) Effects of build orientation and heat treatments on the tensile and fracture toughness properties of additively manufactured AlSi10Mg. *International Journal of Mechanical Sciences*
- ASTM (2017) Standard Test Methods for Density of Compacted or Sintered Powder Metallurgy (PM) Products Using Archimedes' Principle. ASTM. <https://doi.org/10.1520/B0962-17>
- ASTM (2020) ASTM E1820-20b Standard Test Method for Measurement of Fracture Toughness. ASTM International
- ASTM (2021) ASTM E8/E8M-21 Standard Test Methods for Tension Testing of Metallic Materials. <https://www.astm.org/Standards/E8>
- Brandl E, Heckenberger U, Holzinger V, Buchbinder D (2012) Additive manufactured alsi10mg samples using selective laser melting (SLM): Microstructure, high cycle fatigue, and fracture behavior. *Materials & Design* 34:159–169
- Casati R, Hamidi Nasab M, Coduri M, Tirelli V, Vedani M (2018) Effects of platform pre-heating and thermal-treatment strategies on properties of alsi10mg alloy processed by selective laser melting. *Metals* 8(11):954
- Casati R, Coduri M, Checchia S, Vedani M (2021) Insight into the effect of different thermal treatment routes on the microstructure of alsi7mg produced by laser powder bed fusion. *Mater Charact* 172:110881. <https://doi.org/10.1016/j.matchar.2021.110881>
- Dowling NE (2013) Mechanical Behavior of Materials: Engineering Methods for Deformation, Fracture, and Fatigue, 4th ed. edn., p. 954. Pearson, Harlow
- Girelli L, Giovagnoli M, Tocci M, Pola A, Fortini A, Merlin M, La Vecchia GM (2019) Evaluation of the impact behaviour of alsi10mg alloy produced using laser additive manufacturing. *Mater Sci Eng, A* 748:38–51
- Herzog D, Seyda V, Wycisk E, Emmelmann C (2016) Additive manufacturing of metals. *Acta Materialia* 117(C), 371–392
- Hitzler L, Hirsch J, Schanz J, Heine B, Merkel M, Hall W, Öchsner A (2019) Fracture toughness of selective laser melted

- AlSi10Mg. Proceedings of the Institution of Mechanical Engineers, Part L: Journal of Materials: Design and Applications 233(4):615–621
- Jang C, Cho P-Y, Kim M, Oh S-J, Yang J-S (2010) Effects of microstructure and residual stress on fatigue crack growth of stainless steel narrow gap welds. *Materials & Design* 31(4):1862–1870
- Kempen K, Thijs L, Van Humbeeck J, Kruth J-P (2012) Mechanical properties of alsi10mg produced by selective laser melting. *Physics Procedia* 39, 439–446. Schmidt, M
- Li W, Li S, Liu J, Zhang A, Zhou Y, Wei Q, Yan C, Shi Y (2016) Effect of heat treatment on alsi10mg alloy fabricated by selective laser melting: Microstructure evolution, mechanical properties and fracture mechanism. *Mater Sci Eng, A* 663:116–125
- Liu Q, Wu H, Paul MJ, He P, Peng Z, Gludovatz B, Kruczic JJ, Wang CH, Li X (2020) Machine-learning assisted laser powder bed fusion process optimization for AlSi10Mg: New microstructure description indices and fracture mechanisms. *Acta Mater* 201:316–328
- McNeill SR, Peters WH, Sutton MA (1987) Estimation of stress intensity factor by digital image correlation. *Eng Fract Mech* 28(1):101–112
- Menezes JTO, Castrodeza EM, Casati R (2019) Effect of build orientation on fracture and tensile behavior of a357 al alloy processed by selective laser melting. *Mater Sci Eng, A* 766:138392
- Menezes JTO, Castrodeza EM, Patriarca L et al (2022) Effect of heat treatments and loading orientation on the tensile properties and fracture toughness of alsi7mg alloy produced by laser powder bed fusion. *Int J Fract* 235:145–157. <https://doi.org/10.1007/s10704-022-00631-5>
- Minerva G, Patriarca L, Foletti S, Beretta S (2022) Static assessment of flawed thin AlSi10Mg parts produced by Laser Powder Bed Fusion. *Materials & Design* 224, 111292 <https://doi.org/10.1016/j.matdes.2022.111292>
- Park T-H, Baek M-S, Hyer H, Sohn Y, Lee K-A (2021) Effect of direct aging on the microstructure and tensile properties of alsi10mg alloy manufactured by selective laser melting process. *Mater Charact* 176:111113
- Paul MJ, Liu Q, Best JP, Li X, Kruczic JJ, Ramamurty U, Gludovatz B (2021) Fracture resistance of alsi10mg fabricated by laser powder bed fusion. *Acta Mater* 211:116869
- Rosenthal I, Shneck R, Stern A (2018) Heat treatment effect on the mechanical properties and fracture mechanism in alsi10mg fabricated by additive manufacturing selective laser melting process. *Mater Sci Eng, A* 729:310–322
- Shifeng W, Shuai L, Qingsong W, Yan C, Sheng Z, Yusheng S (2014) Effect of molten pool boundaries on the mechanical properties of selective laser melting parts. *J Mater Process Technol* 214(11):2660–2667
- Suryawanshi J, Prashanth KG, Scudino S, Eckert J, Prakash O, Ramamurty U (2016) Simultaneous enhancements of strength and toughness in an al-12si alloy synthesized using selective laser melting. *Acta Mater* 115:285–294
- Takata N, Kodaira H, Sekizawa K, Suzuki A, Kobashi M (2017) Change in microstructure of selectively laser melted alsi10mg alloy with heat treatments. *Mater Sci Eng, A* 704:218–228
- Tang H, Gao C, Zhang Y, Zhang N, Lei C, Bi Y, Tang P, Rao JH (2023) Effects of direct aging treatment on microstructure, mechanical properties and residual stress of selective laser melted alsi10mg alloy. *Journal of Materials Science & Technology* 139:198–209
- Trudel A, Lévesque M, Brochu M (2014) Microstructural effects on the fatigue crack growth resistance of a stainless steel ca6nm weld. *Eng Fract Mech* 115:60–72
- Xiong ZH, Liu SL, Li SF, Shi Y, Yang YF, Misra RDK (2019) Role of melt pool boundary condition in determining the mechanical properties of selective laser melting alsi10mg alloy. *Mater Sci Eng, A* 740–741:148–156
- Xu Z, Liu A, Wang X (2019) The influence of building direction on the fatigue crack propagation behavior of ti6al4v alloy produced by selective laser melting. *Mater Sci Eng, A* 767:138409
- Zhai Y, Lados DA, LaGoy JL (2014) Additive manufacturing: making imagination the major limitation. *JOM* 66(5):808–816
- Zhang L, Zhong H, Li S, Zhao H, Chen J, Qi L (2020) Microstructure, mechanical properties and fatigue crack growth behavior of friction stir welded joint of 6061–t6 aluminum alloy. *Int J Fatigue* 135:105556
- Zhao L, Song L, Macías JGS, Zhu Y, Huang M, Simar A, Li Z (2022) Review on the correlation between microstructure and mechanical performance for laser powder bed fusion alsi10mg. *Additive Manufacturing*, 102914

Publisher's Note Springer Nature remains neutral with regard to jurisdictional claims in published maps and institutional affiliations.